*energies*

MDPI

*Article*

# Numerical Simulation of Well Type Optimization in Tridimensional Development of Multi-Layer Shale Gas Reservoir

**Tao Huang [1,*], Xin Liao [1], Zhaoqin Huang [2], Fuquan Song [1] and Renyi Wang [1]**

[1] School of Petrochemical Engineering & Environment, Zhejiang Ocean University, Zhoushan 316022, China
[2] School of Petroleum Engineering, China University of Petroleum (East China), Qingdao 266580, China
* Correspondence: huangtao@zjou.edu.cn

**Abstract:** Aimed at the development of shale gas reservoirs with large reservoir thickness and multiple layers, this paper carried out a numerical simulation study on the optimization of three different well types: horizontal well, deviated well, and vertical well. To make the model more in line with the characteristics of shale gas reservoirs, a two-phase gas–water seepage mathematical model of shale gas reservoirs was established, considering the adsorption and desorption of shale gas, Knudsen diffusion effect, and stress sensitivity effect. The embedded discrete fracture model was used to describe hydraulic fracture and natural fracture. Based on Fortran language, a numerical simulator for multi-layer development of shale gas reservoirs was compiled, and the calculation results were compared with the actual production data of Barnett shale gas reservoirs to verify the reliability of the numerical simulator. The spread range of hydraulic fractures in the reservoir with different natural fracture densities is calculated by the simulation to determine well spacing and fracture spacing. The orthogonal experimental design method is then used to optimize the best combination of well spacing and fracture spacing for different well types. The results show that the well productivity of the high-density (0.012 $m/m^2$) natural fractures reservoir > the well productivity of the medium-density (0.006 $m/m^2$) natural fractures reservoir > the well productivity of the low-density (0.001 $m/m^2$) natural fractures reservoir. According to the design of the orthogonal test, it can be seen that the most significant factor affecting the productivity of horizontal wells is the fracture spacing in the Y direction. For deviated wells and vertical wells, the X-direction well spacing has the greatest impact on its productivity.

**Keywords:** shale gas reservoir; multi-layer development; numerical simulation; well-type optimization

check for updates

**Citation:** Huang, T.; Liao, X.; Huang, Z.; Song, F.; Wang, R. Numerical Simulation of Well Type Optimization in Tridimensional Development of Multi-Layer Shale Gas Reservoir. *Energies* **2022**, *15*, 6529. https://doi.org/10.3390/en15186529

Academic Editor: Reza Rezaee

Received: 13 August 2022
Accepted: 2 September 2022
Published: 7 September 2022

**Publisher's Note:** MDPI stays neutral with regard to jurisdictional claims in published maps and institutional affiliations.

**Copyright:** © 2022 by the authors. Licensee MDPI, Basel, Switzerland. This article is an open access article distributed under the terms and conditions of the Creative Commons Attribution (CC BY) license (https://creativecommons.org/licenses/by/4.0/).

## 1. Introduction

With the sharp decline in reserves and productivity of conventional oil and gas resources, in recent years shale gas has gradually become an important supplement to traditional energy [1]. However, compared with conventional gas reservoirs, shale gas reservoirs generally have ultra-low porosity and permeability. The porosity is usually less than 10%, the permeability varies from micro-Darcy to nano-Darcy, and the reservoir heterogeneity is serious, requiring hydraulic fracturing to enable commercial exploitation [2,3]. Hydraulic fracturing and horizontal drilling are key technologies for shale gas production in most shale reservoirs [4]. Shale gas mainly exists in the two forms of free state and adsorption state in the reservoir. It exists in the matrix pores and natural fractures in the free state, while it is adsorbed on the surface of organic matter in the adsorption state [5]. The existence mode of shale gas and the characteristics of shale gas reservoirs mean that there are multiple migration mechanisms of shale gas in the reservoir, such as Knudsen diffusion, stress sensitivity effect, and adsorption and desorption of adsorbed gas in the production process [6].

In shale gas reservoirs, when the average pore radius is comparable to the mean free path of gas molecules, Knudsen diffusion must be considered in the gas flow matrix. Knudsen diffusion will change the apparent permeability of the matrix to affect shale gas production, and the smaller the shale pore radius, the more obvious the impact on production. Under the effect of surface diffusion and Knudsen diffusion, the apparent permeability of the shale matrix increases, which increases the cumulative gas production of shale gas [7–9]. In conventional oil and gas reservoirs, the influence of geomechanics on rock deformation or permeability is usually small, which is mostly ignored in actual production. However, in shale gas reservoirs with nanoscale pores or micro-fractures, geomechanical effects may be relatively large and may have a significant impact on fracture and matrix permeability [10]. Wang et al. [11] showed that the permeability in the Marcellus shale is related to pressure, and the influence of confining pressure on permeability is caused by the decrease of porosity and decreases with the increase in confining pressure. Bustin et al. [12] reported the strong effect of stress (confining pressure) on permeability in Barnett, Muskwa, and Ohio shales, and showed that the degree of permeability reduction with confining pressure is significantly higher in shales than in consolidated sandstone or carbonate. The natural gas in shale gas reservoirs exists in the form of the free phase, and also in the form of adsorbed gas. The adsorbed gas accounts for a large proportion of the total natural gas reserves (20–80%), which is also an important factor affecting recovery [13]. Moreover, adsorption–desorption is an important occurrence form of shale gas, and adsorption gas is a supplement to free gas in the development process, which has a significant impact on the unsteady production capacity in the middle and late stages of gas well production [14]. During the exploitation of shale gas reservoirs, the adsorption and desorption of shale gas will also lead to dynamic changes in the effective pore radius of the shale matrix, thereby affecting the apparent permeability [15]. Therefore, to make the model accurately simulate shale gas productivity, the percolation mechanism of shale gas must be comprehensively considered.

The combination of horizontal drilling and hydraulic fracturing is the key technology for shale gas production. Although hydraulic fracturing can increase the production of shale gas wells, the operating cost is high. Due to the high cost of drilling and completion, the economy of gas wells will be affected by their performance, so the analysis and optimization of well parameters (such as well spacing and fracture spacing) are very important [16,17]. Rafiee et al. [18] proposed two new designs for horizontal wells and improved well performance from both rock mechanics and fluid production, but only a 500-foot fracture spacing was assumed, without optimizing both well location and fracture spacing. Diaz de Souza et al. [19] studied the sensitivity of horizontal well layout in Haynesville shale to obtain the best well spacing. However, the optimization of key parameters of economic development zones, such as fracture spacing and fracture half-length, has not been considered. Wei Yu et al. [20] used the corresponding surface method, based on the net present value, and optimized the fracturing design and the layout of multiple wells at the same time, providing a theoretical reference for the effective exploitation of shale gas reservoirs. Ramanathan et al. [21] used the unconventional fracture model to predict the production performance of multiple well groups with different fracture geometries and points out that the interference between well groups makes the well spacing and the number of fracturing fractures important optimal values. To improve shale gas recovery and reduce engineering costs, it is still necessary to comprehensively optimize the relevant parameters of wells. However, at the same time, for large thickness shale reservoirs, there are few numerical simulation studies on well-type optimization of horizontal wells, deviated wells, and vertical wells.

In this paper, we establish a mathematical model of shale gas reservoir seepage that considers adsorption and desorption, Knudsen diffusion, and shale reservoir stress sensitivity effects and compiles a corresponding numerical simulator based on Fortran language. Firstly, the spread range of hydraulic fractures in the reservoir with different natural fracture densities is calculated by the simulation to determine well spacing and

fracture spacing. The orthogonal experimental design method is then used to optimize the best combination of well spacing and fracture spacing for different well types, thereby providing a theoretical basis for well type optimization for the multi-layer development of on-site shale gas reservoirs.

## 2. Mathematical Model Descriptions

### *2.1. Fluid-Governing Equations*

There are many occurrence modes of shale gas, among which the gas present in the adsorption state on the surface of the pores between the particles is called adsorbed gas. Affected by temperature and pressure, the adsorbed gas will be desorbed into free gas [22]. In this study, it is assumed that only gas and water components exist in shale gas reservoirs, while adsorbed gas exists in the solid phase of rock [23], and its general integral form is:

$$\frac{\partial}{\partial t}\int_{\Omega} A_\beta d\Omega + \int_{\Gamma} F_\beta \cdot n d\Gamma = \int_{\Omega} q_\beta d\Omega \tag{1}$$

where $n$ is the unit normal vector of boundary $\Gamma$, $A$ is the mass per unit volume, $F$ is mass flux, and $q$ is the source terms on domain $\Omega$. The mass per unit volume is expressed as:

$$\begin{cases} A_\beta = \phi S_\beta \rho_\beta + m_\beta \text{ , in matrix} \\ A_\beta = \phi S_\beta \rho_\beta \text{ , in fracture} \end{cases} \tag{2}$$

where subscript $\beta$ indicates fluid phases (water or gas), $\phi$ is the effective porosity of the porous or fractured media, $\rho_\beta$ is the density of fluid, $m_\beta$ is the adsorption/desorption mass term for the gas component per unit volume of formation, and $S_\beta$ is the saturation of phase $\beta$.

$$S_g + S_w = 1, \qquad p_c(S_w) = p_g - p_w \tag{3}$$

$$\rho_w = \rho_{w0}\exp[c_w(p_w - p_{w0})], \quad \rho_g = \frac{p_g M_g}{Z_g R T} \tag{4}$$

where the subscript 0 indicates the initial state, $c_w$ is the compression coefficient of water, $p_c$ is the capillary pressure, $p_g$ and $p_w$ are the pressure of gas and water, respectively, $M_g$ is the molar mass of gas, $Z_g$ is the gas compression factor, $R$ is the general gas constant, and $T$ is the reservoir temperature.

The amount of adsorbed gas is determined according to the Langmuir isotherm as a function of gas pressure.

The gas compressibility factor, $Z_g$ can be calculated based on the following equations [24]:

$$Z_g = \left(0.702e^{-2.5T_{pr}}\right)p_{pr}^2 - 5.524e^{-2.5T_{pr}}p_{pr} + 0.044T_{pr}^2 - 0.164T_{pr} \tag{5}$$

where $p_{pr}$ and $T_{pr}$ indicate the pseudo-reduced pressure and pseudo-reduced temperature, respectively.

The Langmuir isotherm function can determine the adsorption capacity of shale gas:

$$m_g = \rho_r \rho_{gstd} V_L \frac{p_g/Z_g}{p_L + p_g/Z_g} \tag{6}$$

where $\rho_r$ is matrix density, $\rho_{gstd}$ is gas density at standard condition, and $V_L$ and $p_L$ are the Langmuir volume and Langmuir pressure, respectively. The mass-flux term in Equation (1) is given by [25,26]:

$$\begin{cases} F_w = -\rho_w \frac{k_{rw}}{u_w} k(\nabla p_w - \rho_w g \nabla D), & \text{in matrix and fracture} \\ F_g = -\rho_g \frac{k_{rg}}{u_g} k_\infty (1 + \alpha(K_n)K_n)\left(1 + \frac{4K_n}{1-bK_n}\right)(\nabla p_g - \rho_g g \nabla D), & \text{in matrix} \\ F_g = -\rho_g \frac{k_{rg}}{u_g} k_\infty (\nabla p_g - \rho_g g \nabla D), & \text{in fracture} \end{cases} \tag{7}$$

where $k$ is the absolute permeability, $k_\infty$ is the intrinsic permeability, which, for simplicity, equals absolute permeability in this study, $k_{r\beta}$ and $\mu_\beta$ are the relative permeability and viscosity of phase $\beta$ (the relative permeabilities are calculated by using the table-lookup approach, in which the correlations between relative permeabilities and water saturation are obtained from laboratory studies), $g$ is gravitational acceleration, $D$ is depth, $b$ is slip coefficient, $K_n$ is Knudsen number and represents the ratio of the average free path of gas molecule to the radius of pore, and $\alpha$ denotes the thinning coefficient, which can be calculated by the following formula [27]:

$$K_n = \frac{\lambda}{r_h}, \quad \alpha = \frac{1.358}{1 + 0.170 K_n{}^{-0.4348}} \tag{8}$$

where $\lambda$ is the average free path of gas molecules and $r_h$ is the average flow radius of gas molecules, and can be calculated by the following formula [27]:

$$\lambda = \frac{k_b T Z_g}{\sqrt{2}\pi {d_m}^2 p_g}, \quad \mathrm{r}_h = 2\sqrt{2\tau_0}\sqrt{\frac{k_\infty}{\phi}} \tag{9}$$

where $k_b$ is Boltzmann constant, $d_m$ is the molecular radius, and $\tau_0$ is the tortuosity of porous media, dimensionless.

### *2.2. Stress Sensitivity Effect of Shale Reservoir*

The traditional percolation theory generally assumes that the porous media skeleton of fluid flow is completely rigid, and this simplification has defects that are not suitable for actual production. Because the porosity of shale reservoirs is extremely low, it is particularly sensitive to reservoir pressure changes. Shale stress sensitivity is a phenomenon by which the effective stress on the rock skeleton increases due to the decrease of reservoir pressure during shale gas exploitation, resulting in changes in physical parameters such as porosity and permeability of shale reservoirs [28,29].

$$\phi(p) = \phi_0 e^{\alpha_\phi (p - p_0)} \tag{10}$$

$$k(p) = k_0 e^{\alpha_k (p - p_0)} \tag{11}$$

where $k(p)$ is reservoir permeability under pressure, $p$, and $p = p_w S_w + p_g S_g$. $p_0$ is the original pressure of the gas reservoir; $\phi(p)$ and $\phi_0$ are the porosity corresponding to $p$ and $p_0$, respectively, and $a_k$ and $a_\phi$ are the permeability and porosity variation coefficient, respectively. As the porosity and permeability of the shale matrix changes with reservoir pressure, the average flow radius, $r_h$, is also dynamic, and its value is updated according to Equation (9).

## 3. Flow Equation Discretization

The structured grids of EDFM are used to explicitly model the fractured shale reservoir. As shown in Figure 1, the matrix region is discretized using an orthogonal structured grid, and the fracture grid is segmented by matrix gridlines. Details are given by Xu et al. [30], Yu et al. [31], and Liu et al. [32].

In this study, using the FVM discrete gas flow governing equations, the time dispersion is approximated by the standard first order [33], and gravity is ignored. Therefore, the residual expression of Equation (1) is:

$$R_{\beta,i}^{n+1} = \left[ \left( \phi S_\beta \rho_\beta + m_\beta \right)_i^{n+1} - \left( \phi S_\beta \rho_\beta + m_\beta \right)_i^n \right] \frac{V_i}{\Delta t} - \sum_{j \in G_i} (\rho\lambda)_{ij+1/2}^{n+1} T_{ij} \left( p_{\beta,j}^{n+1} - p_{\beta,i}^{n+1} \right) - q_{\beta,i}^{n+1} V_i \tag{12}$$

where $n$ is the time level, $i$ and $j$ are element numbers, $\Delta t$ is the time step, $V$ is the element volume, $G_i$ is the adjacent element set of element $i$, $ij + 1/2$ represents the upstream weight

value on the interface between elements $i$ and $j$, $\lambda = \frac{1}{\mu}$ is the gas mobility, and $T_{ij}$ is the transmissibility between element $i$ and $j$, defined as:

$$T_{ij} = \frac{A_{ij} k_{ij+1/2}}{d_i + d_j} \tag{13}$$

where $A_{ij}$ is the interface area, $d_i$ and $d_j$ are vertical distances from the cell center to the interface, and $k_{ij+1/2}$ is an averaged absolute permeability. To include the Knudsen effect on gas flow, the permeability in Equation (11) should be evaluated as $(k(1+\alpha K_n)(1+4K_n/1-bK_n))_{ij+1/2}$. In this study, the fluid flow in fractures is modeled explicitly with the embedded-discrete-fracture model. The upstream-weighting is applied for the mobility and transmissibility terms.

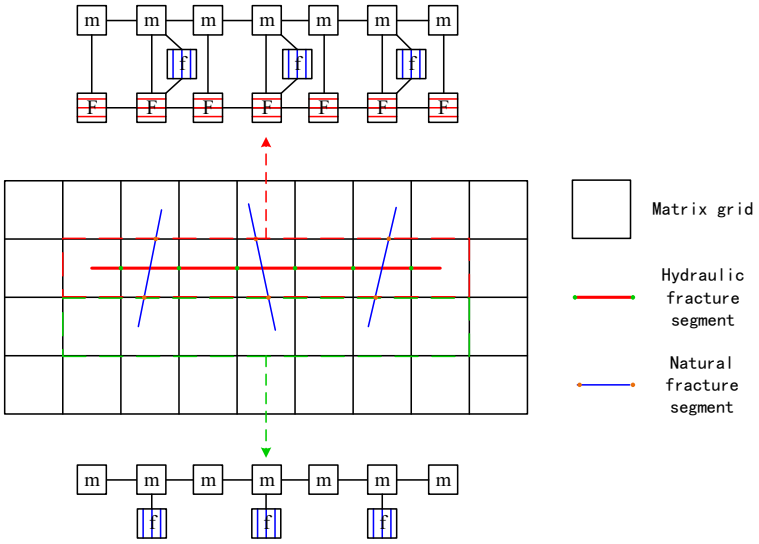


**Figure 1.** Schematic of fractured-shale-reservoir discretization: m = matrix; F = hydraulic fracture; f = natural fracture.

In addition, in this paper, the outer boundary conditions of the model are closed boundary conditions:

$$\left.\frac{\partial P_m}{\partial n}\right|_{\Gamma_1} = \left.\frac{\partial P_f}{\partial_n}\right|_{\Gamma_1} = 0 \tag{14}$$

The internal boundary condition is the constant pressure boundary condition:

$$P|_{\Gamma_2} = P_w \tag{15}$$

In the formula, $\Gamma_1$ and $\Gamma_2$ denote the outer boundary and the inner boundary, respectively, $n$ represents the normal unit vector of the outer boundary, and $P_w$ is the bottom hole flowing pressure, MPa.

## 4. Model Verification

To verify the accuracy of the new model, a well in the Barnett shale gas reservoir was selected, and parameters related to the Barnett shale gas reservoir are shown in Table 1. The reservoir parameters for Barnett shale were obtained from the literature [34,35]. The simulation calculated daily gas production for 1600 days and compared it with actual daily gas production from the Barnett shale gas reservoir.

**Table 1.** Parameters related to the Barnett Shale gas reservoir.

| Parameter | Value | Units |
|---|---|---|
| 3D model size | 1100 × 290 × 90 | m |
| Initial reservoir pressure | 25 | MPa |
| Bottom hole pressure | 2.5 | MPa |
| Langmuir pressure | 4.48 | MPa |
| Langmuir volume | $2.72 \times 10^{-3}$ | $m^3/kg$ |
| Reservoir temperature | 340 | K |
| Well radius | 0.1 | m |
| Reservoir porosity | 0.06 | Dimensionless |
| Initial permeability | $1.4 \times 10^{-19}$ | $m^2$ |
| Hydraulic fracture half-length | 40 | m |
| Hydraulic fracture spacing | 30 | m |
| Number of hydraulic fractures | 28 | Dimensionless |
| Hydraulic fracture height | 90 | m |
| Length of horizontal well | 900 | m |
| Shale density | 2580 | $kg/m^3$ |
| Initial gas saturation | 0.776 | Fraction |
| Initial water saturation | 0.224 | Fraction |
| Gas viscosity | $2.01 \times 10^{-5}$ | Pa·s |
| Natural fracture permeability | $1 \times 10^{-13}$ | m |
| Hydraulic fracture permeability | $1.17 \times 10^{-11}$ | m |
| Compression coefficient of water | $4.4 \times 10^{-10}$ | $Pa^{-1}$ |
| Porosity variation coefficient | 0.08 | $Pa^{-1}$ |
| Permeability variation coefficient | 0.62 | $Pa^{-1}$ |

A simulation model was established based on a horizontal well in the Barnett shale gas reservoir, as shown in Figure 2, where the model size (x × y × z) is 1100 m × 290 m × 90 m.

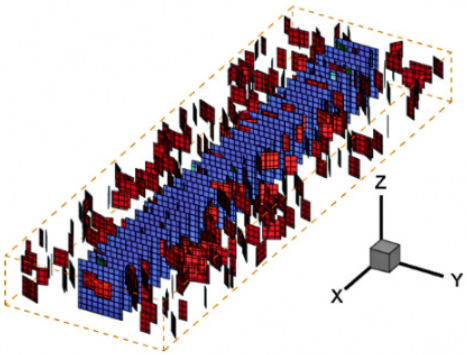


**Figure 2.** 3D schematic diagram of Barnett gas well model.

The pressure, water saturation, and gas saturation distributions of the model in different production periods of 1600 days is shown in Figure 3, and the fitting results of daily gas production are shown in Figure 4.

The root mean square method was used to calculate the fitting rate, and the fitting rate between the simulation results and the actual gas production of the Barnett shale gas reservoir reached 86.4%, which verifies the correctness and reliability of the numerical simulator.

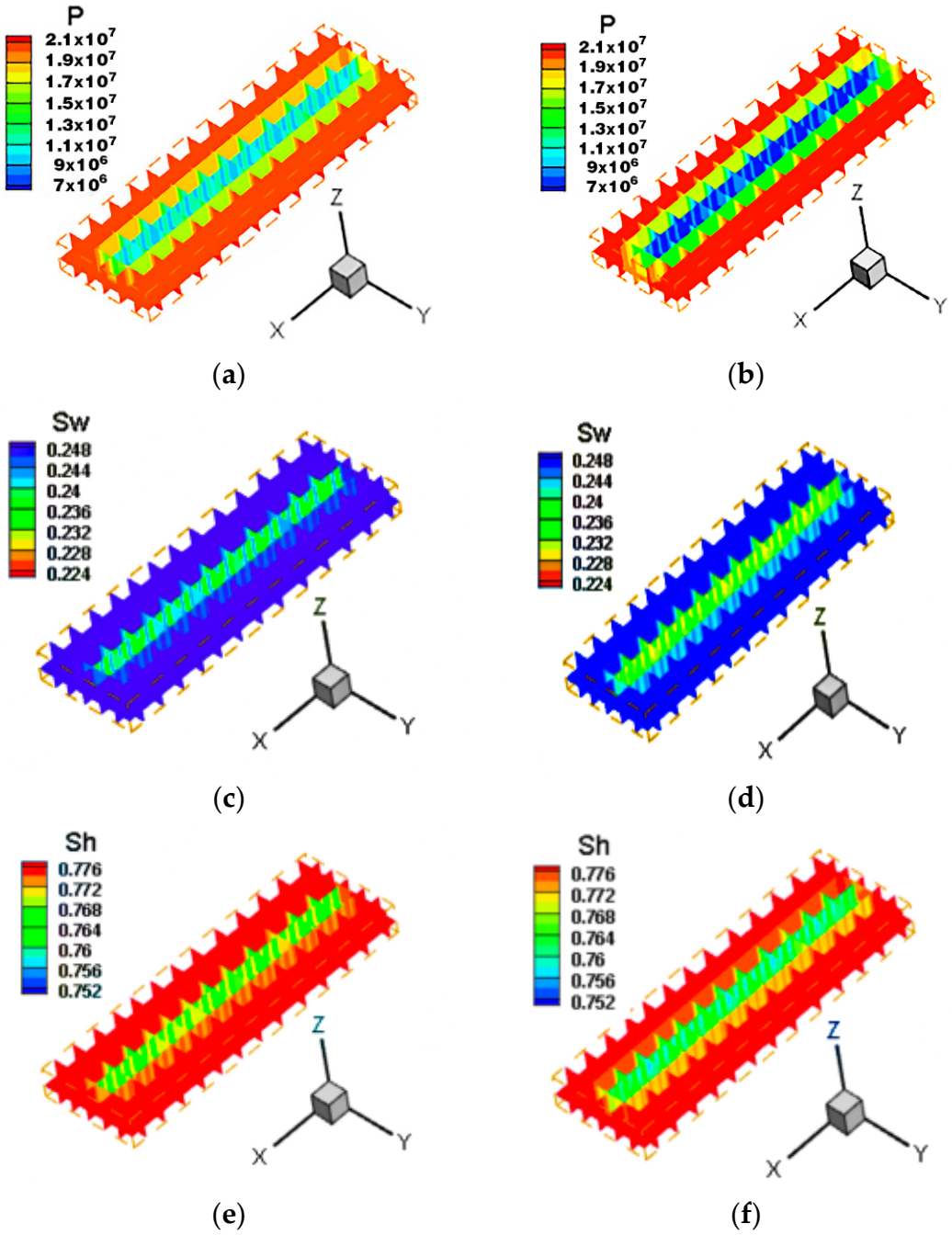


**Figure 3.** Pressure, water saturation, and gas saturation field diagrams of Barnett horizontal well in different production periods: (**a**) Pressure distribution of Barnett horizontal well over 800 days of production; (**b**) Pressure distribution of Barnett horizontal well over 1600 days of production; (**c**) water saturation distribution of Barnett horizontal well over 800 days of production; (**d**) water saturation distribution of Barnett horizontal well over 1600 days of production; (**e**) gas saturation distribution of Barnett horizontal well over 800 days of production; (**f**) gas saturation distribution of Barnett horizontal well over 1600 days of production.

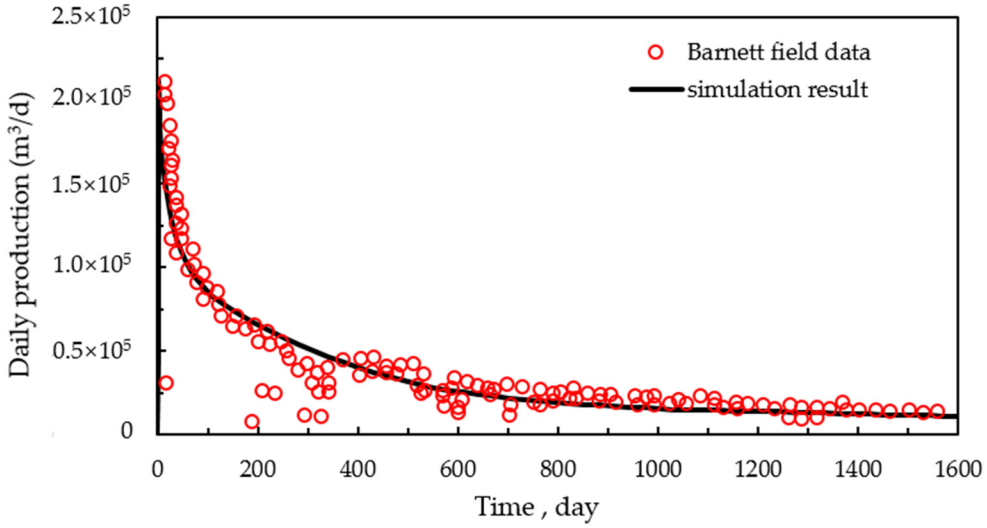


**Figure 4.** Comparison between field data and simulation results in Barnett Shale.

## 5. Results and Discussion

First, the utilization range of hydraulic fractures under different natural fracture densities is calculated, and then the well spacing and fracture spacing in the X, Y, and Z directions of horizontal wells, deviated wells, and vertical wells are determined according to the calculation results. The optimal well spacing and fracture spacing of each well type are optimized by orthogonal experimental design.

### *5.1. Calculation of Reservoir Utilization Range under Different Natural Fracture Densities*

According to the field data, a set of gas reservoir parameters are selected: the initial formation pressure is 38.55 MPa, bottom hole pressure is 10 MPa, wellbore radius is 0.1 m, and formation water viscosity is 0.50 mPa·s. Irreducible water saturation is 0.18. The hydraulic fracture permeability and natural fracture permeability are $1.17 \times 10^{-11}$ m, and $1 \times 10^{-13}$ m, respectively. Matrix density is 2800 kg/m$^3$, Langmuir volume is $8 \times 10^{-4}$ m$^3$/kg, and Langmuir pressure is 15 MPa. In the established numerical simulation model, the hydraulic fracture height is 20 m, and the properties of each layer and the development of natural fractures are shown in Table 2.

**Table 2.** Properties of each layer and development of natural fractures.

| Layer Number | Layer Thickness/m | Porosity | Water Saturation | Gas Saturation | Matrix Permeability/$10^{-3}$ mD | Natural Fracture Density/m/m$^2$ |
|---|---|---|---|---|---|---|
| 1 | 20 | 0.028 | 0.25 | 0.75 | 0.326 | 0.012 |
| 2 | 45 | 0.025 | 0.23 | 0.77 | 0.407 | 0.012 |
| 3 | 40 | 0.022 | 0.22 | 0.78 | 0.172 | 0.006 |
| 4 | 50 | 0.034 | 0.24 | 0.76 | 0.150 | 0.006 |
| 5 | 40 | 0.038 | 0.21 | 0.79 | 0.180 | 0.006 |
| 6 | 30 | 0.022 | 0.30 | 0.70 | 0.137 | 0.001 |
| 7 | 35 | 0.015 | 0.21 | 0.79 | 0.133 | 0.001 |

To determine the well spacing and hydraulic fracture spacing under different natural fracture densities, the pressure change range after 15 years of exploitation is calculated, and the reservoir utilization range under high-density (0.012 m/m$^2$), medium-density (0.006 m/m$^2$), and low-density (0.001 m/m$^2$) natural fractures are obtained (Figures 5–7), so as to determine the well spacing and fracture spacing in the various directions of different well types.

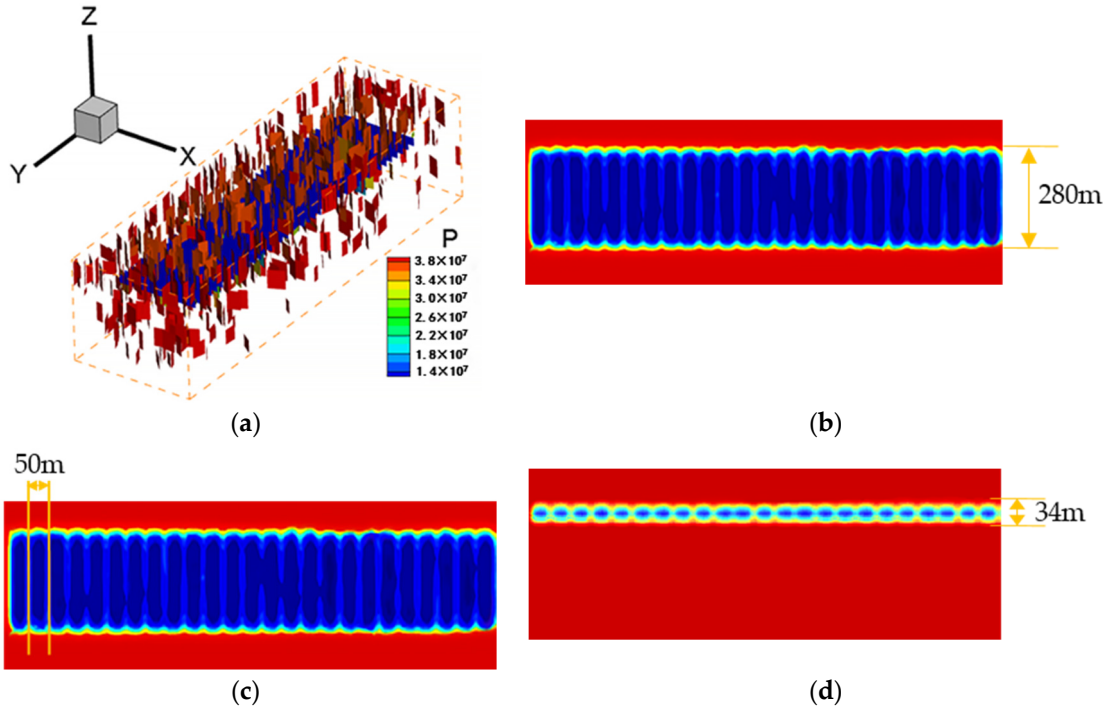


**Figure 5.** Pressure changes and reservoir utilization range after 15 years of high-density (0.012 m/m$^2$) natural fracture reservoir exploitation: (**a**) Pressure field diagram; (**b**) Utilization range in X direction; (**c**) Utilization range in Y direction; (**d**) Utilization range in Z direction.

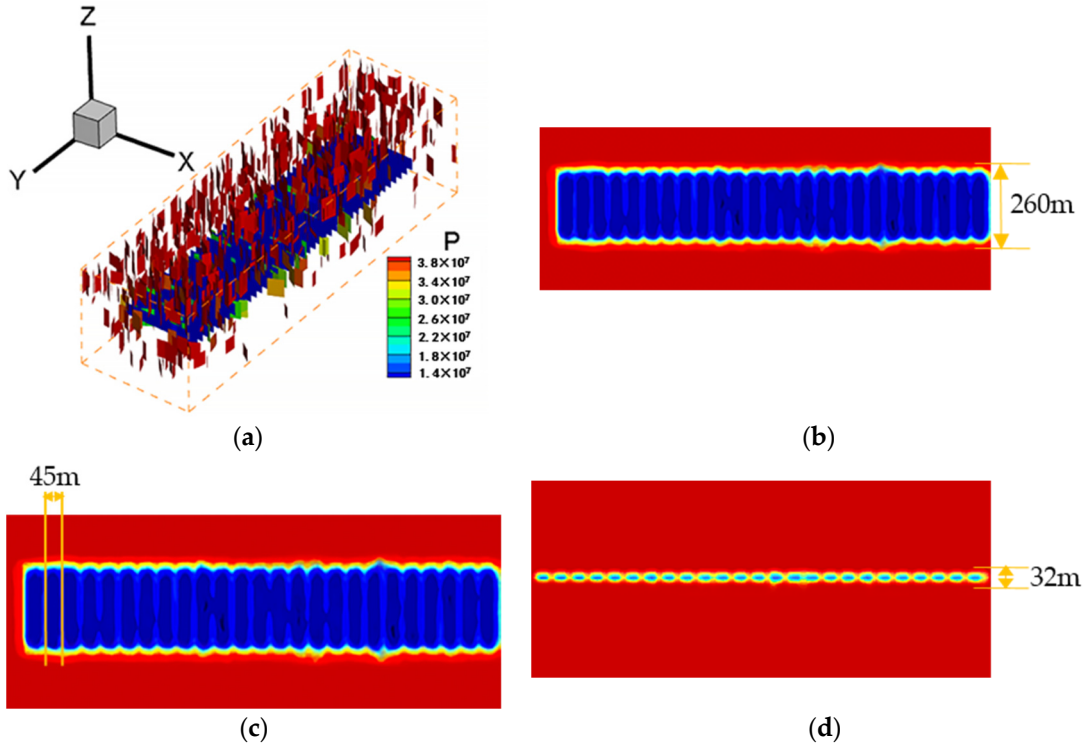


**Figure 6.** Pressure changes and reservoir utilization range after 15 years of medium-density (0.006 m/m$^2$) natural fracture reservoir exploitation: (**a**) Pressure field diagram; (**b**) Utilization range in X direction; (**c**) Utilization range in Y direction; (**d**) Utilization range in Z direction.

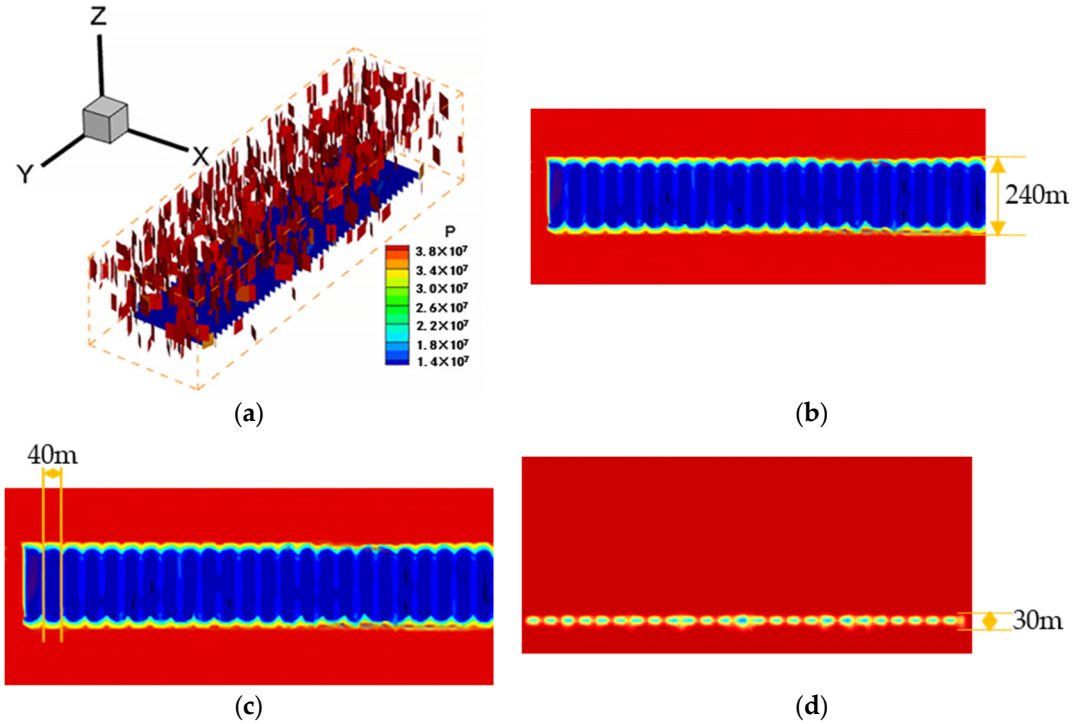


**Figure 7.** Pressure changes and reservoir utilization range after 15 years of low-density (0.001 m/m$^2$) natural fracture reservoir exploitation: (**a**) Pressure field diagram; (**b**) Utilization range in X direction; (**c**) Utilization range in Y direction; (**d**) Utilization range in Z direction.

From the simulation results, it can be seen that, for reservoirs with high-density, medium-density, and low-density natural fracture after 15 years of exploitation, the reservoir utilization ranges in the X direction are 280 m, 260 m, and 240 m, in the Y direction they are 50 m, 45 m, and 40 m, and in the Z direction they are 34 m, 32 m, and 30 m.

Figure 8 shows the production of the well at high-density, medium-density, and low-density natural fractures. As shown above, the density of natural fractures affects the productivity of the well. The well productivity of the high-density (0.012 m/m$^2$) natural fractures reservoir > the well productivity of the medium-density (0.006 m/m$^2$) natural fractures reservoir > the well productivity of the low-density (0.001 m/m$^2$) natural fractures reservoir.

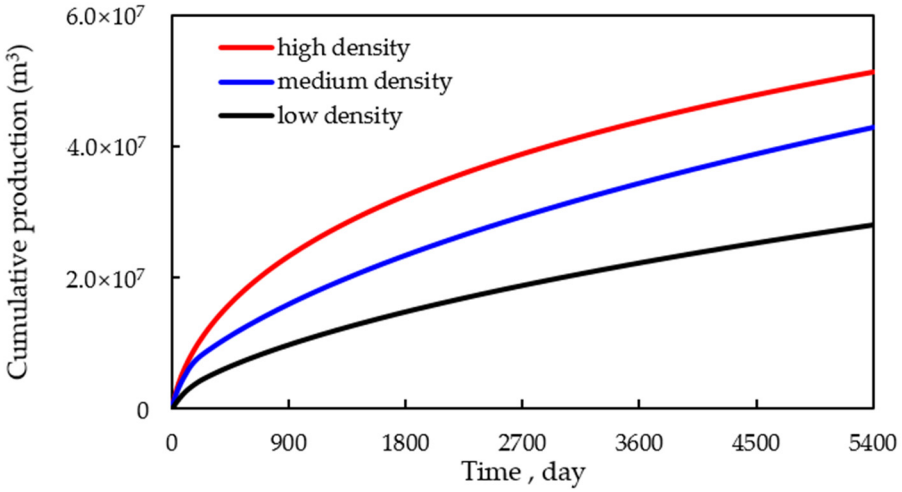


**Figure 8.** Cumulative production of the well in high, medium, and low fracture density.

### *5.2. Productivity Evaluation and Optimization of Different Well Types*

A shale gas reservoir model is established to simulate the fracturing production of horizontal wells, deviated wells, and vertical wells. The model size (x × y × z) is 1200 m × 1500 m × 260 m. The properties of each layer and the development of natural fractures are shown in Table 2, and the related parameters of wells and fractures are shown in Table 3. The model permeability field diagram, model porosity field diagram, horizontal well layout diagram, deviated well layout diagram, and vertical well layout diagram are shown in Figure 9.

**Table 3.** Well and hydraulic fracture related parameters.

| Essential Parameter | Value | Units |
|---|---|---|
| Initial reservoir pressure | 38.5 | MPa |
| Bottom hole pressure | 10 | MPa |
| Shale density | 2800 | $kg/m^3$ |
| Hydraulic fracture half-length | 100 | m |
| Hydraulic fracture height | 20 | m |
| Initial gas saturation | 0.776 | Fraction |
| Initial water saturation | 0.224 | Fraction |
| Gas viscosity | $2.0 \times 10^{-5}$ | Pa·s |
| Natural fracture permeability | $1 \times 10^{-13}$ | m |
| Hydraulic fracture permeability | $1.17 \times 10^{-11}$ | m |
| Porosity variation coefficient | 0.08 | $Pa^{-1}$ |
| Permeability variation coefficient | 0.62 | $Pa^{-1}$ |

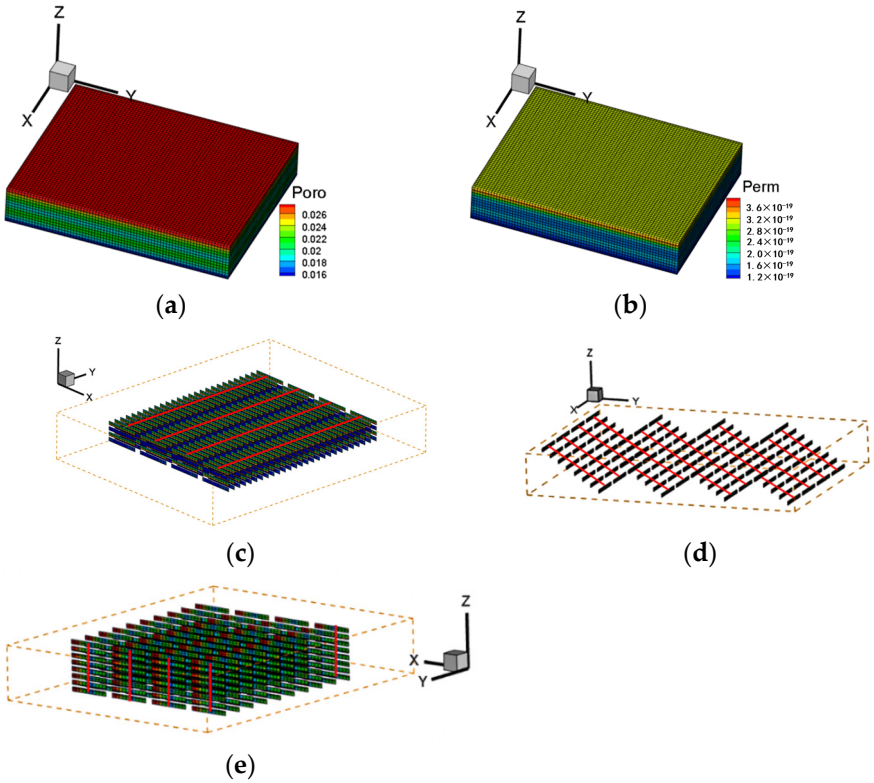


**Figure 9.** (**a**) model porosity field diagram; (**b**) model permeability field diagram; (**c**) horizontal well layout diagram; (**d**) deviated well layout diagram; (**e**) vertical well layout diagram.

#### 5.2.1. Production Capacity Evaluation and Optimization of Horizontal Wells

According to the reservoir utilization range determined in the previous section, for a horizontal well, the well spacings in the X direction are set as 240, 260, and 280 m; the fracture spacings in the Y direction are set as 40, 45, and 50 m; and the well spacings in the Z

direction are set as 30, 32, and 34 m. The reservoir properties and hydraulic fracture-related parameters in the model are from Tables 2 and 3. The above three factors are combined, and the orthogonal design test method is used to determine the optimization scheme, as shown in Table 4.

**Table 4.** Orthogonal design table of horizontal wells.

| Level | Factor | | |
|---|---|---|---|
| | **Factor 1**<br>**X Direction Well Spacing/m** | **Factor 2**<br>**Y Direction Fracture Spacing/m** | **Factor 3**<br>**Z Direction Well Spacing/m** |
| 1 | 240 | 40 | 30 |
| 2 | 260 | 45 | 32 |
| 3 | 280 | 50 | 34 |

According to the orthogonal design method, nine schemes are simulated respectively. Figure 10 is the pressure distribution field diagram of different development schemes for horizontal wells after 20 years of exploitation, and Figure 11 is the cumulative production of a single well with different development schemes of horizontal wells.

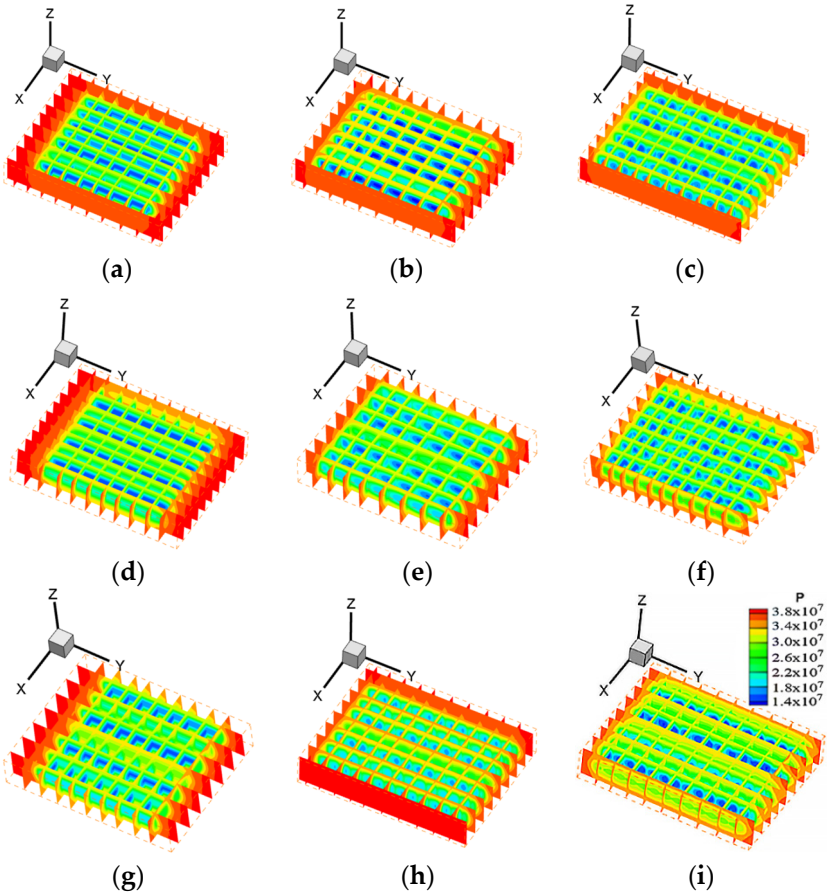


**Figure 10.** Horizontal well pressure distribution field diagram after different development schemes.(**a**) scheme 1; (**b**) scheme 2; (**c**) scheme 3; (**d**) scheme 4; (**e**) scheme 5; (**f**) scheme 6; (**g**) scheme 7; (**h**) scheme 8; (**i**) scheme 9.

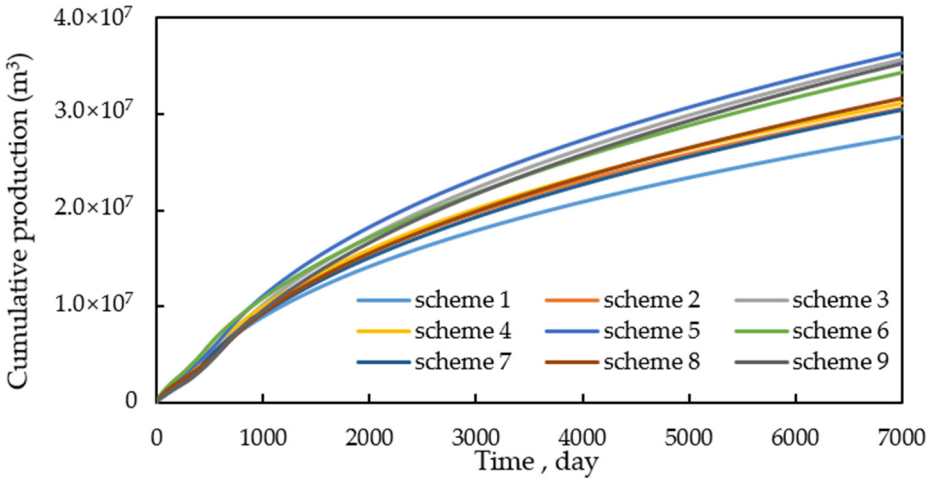


**Figure 11.** Cumulative gas production curve of single well after different development schemes of horizontal well.

Table 5 is the production analysis table of different schemes of horizontal wells.

**Table 5.** Production analysis table for different schemes of horizontal well.

| Orthogonal Design Table | | | | Well Production $10^7$ $m^3$ |
|---|---|---|---|---|
| **Scheme** | **Factor-1** | **Factor-2** | **Factor-3** | |
| 1 | 1 | 1 | 1 | 2.76 |
| 2 | 1 | 2 | 2 | 3.06 |
| 3 | 1 | 3 | 3 | 3.56 |
| 4 | 2 | 1 | 2 | 3.11 |
| 5 | 2 | 2 | 3 | 3.63 |
| 6 | 2 | 3 | 1 | 3.43 |
| 7 | 3 | 1 | 3 | 3.04 |
| 8 | 3 | 2 | 1 | 3.16 |
| 9 | 3 | 3 | 2 | 3.52 |

According to the production values of the above scheme, the average production values, $K_{avg}$ (the average value of well production corresponding to different factor levels), of three levels in the three factors are calculated, as shown in Figure 12. The optimal combination of horizontal well development is 260 m in the well spacing in the X direction, 50 m in the fracture spacing in the Y direction, and 34 m in the well spacing in the Z direction.

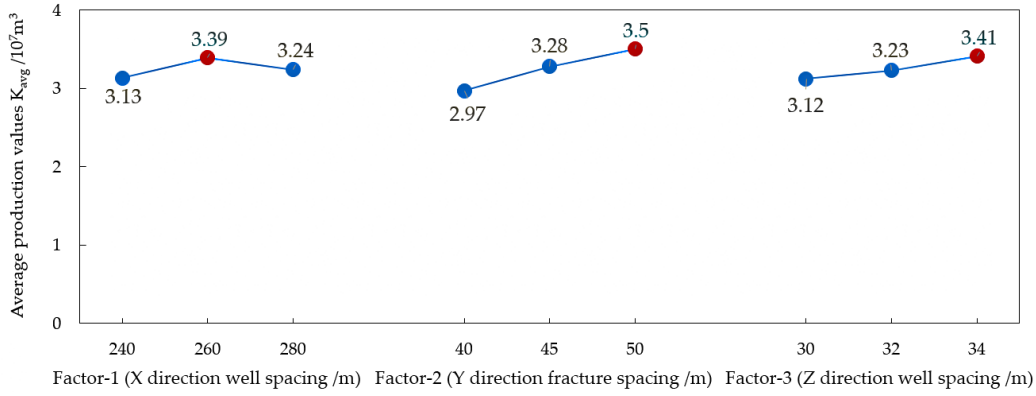


**Figure 12.** Average production values of three levels in the three factors of horizontal well.

By calculating the range value, $R$, of three factors (Maximum average production value minus Minimum average production value), we get $R_{Factor\text{-}2}(0.53) > R_{Factor\text{-}3}(0.29) > R_{Factor\text{-}1}(0.26)$.

Therefore, the most significant factor affecting the productivity of horizontal wells is factor-2 (fracture spacing in the Y direction).

#### 5.2.2. Production Capacity Evaluation and Optimization of Deviated Wells

Based on the same gas reservoir model in the above section, a 45-degree deviated well is used for development. X direction well spacing is set at 240, 260, and 280 m; Y direction fracture spacing at 40, 45, and 50 m; and Z direction fracture spacing at 30, 32, and 34 m. The above three factors are combined, and the optimization scheme is determined by the orthogonal design method, as shown in Table 6.

**Table 6.** Orthogonal design table of deviated wells.

| Level | Factor | | |
|---|---|---|---|
| | **Factor 1**<br>**X Direction Well Spacing/m** | **Factor 2**<br>**Y Direction Fracture Spacing/m** | **Factor 3**<br>**Z Direction Fracture Spacing/m** |
| 1 | 240 | 40 | 30 |
| 2 | 260 | 45 | 32 |
| 3 | 280 | 50 | 34 |

According to the orthogonal design, nine schemes are simulated respectively. Figure 13 is the pressure distribution field diagram of different development schemes for deviated wells after 20 years of exploitation, and Figure 14 is the cumulative production of a single well with different development schemes of deviated wells.

Table 7 is the yield analysis table of the different schemes of deviated wells.

**Table 7.** Yield analysis table for different schemes of deviated well.

| Orthogonal Design Table | | | | Well Yield $10^7$ $m^3$ |
|---|---|---|---|---|
| **Scheme** | **Factor-1** | **Factor-2** | **Factor-3** | |
| 1 | 1 | 1 | 1 | 3.13 |
| 2 | 1 | 2 | 2 | 3.09 |
| 3 | 1 | 3 | 3 | 3.14 |
| 4 | 2 | 1 | 2 | 3.34 |
| 5 | 2 | 2 | 3 | 3.31 |
| 6 | 2 | 3 | 1 | 3.32 |
| 7 | 3 | 1 | 3 | 3.26 |
| 8 | 3 | 2 | 1 | 3.11 |
| 9 | 3 | 3 | 2 | 3.21 |

According to the yield values of the above scheme, the average yield values, $K_{avg}$, of three levels in the three factors are calculated respectively. As shown in Figure 15, the optimal combination of deviated well development is 260 m in the well spacing in the X direction, 40 m in the fracture spacing in the Y direction, and 34 m in the fracture spacing in the Z direction.

By calculating the range value, $R$, of three factors, for deviated wells, we get $R_{Factor\text{-}1}(0.20) > R_{Factor\text{-}2}(0.07) > R_{Factor\text{-}3}(0.05)$. Therefore, factor-1 (X direction well spacing) has the greatest impact on its productivity.

#### 5.2.3. Production Capacity Evaluation and Optimization of Vertical Well

Based on the same gas reservoir model above, for vertical well development. X direction well spacing is set at 240, 260, and 280 m; Y direction well spacing at 40, 45, and 50 m; and Z direction fracture spacing at 30, 32, and 34 m. The above three factors are combined, and the optimization scheme is determined by the orthogonal design method, as shown in Table 8.

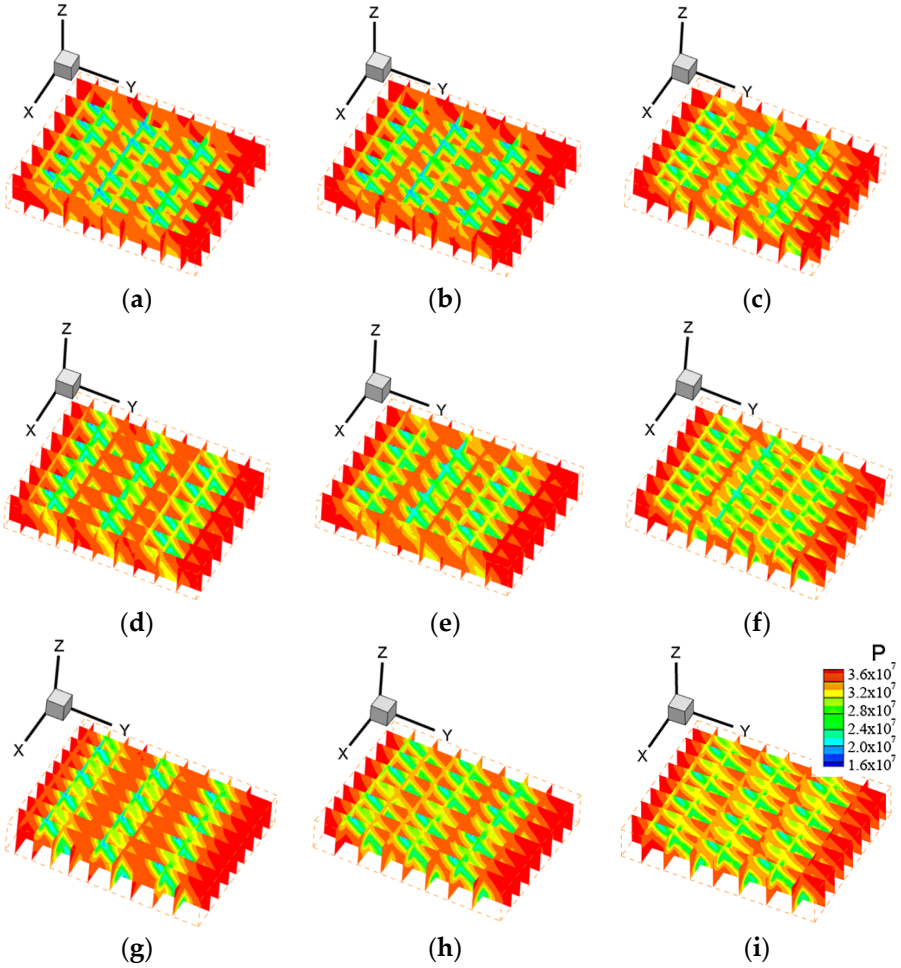


**Figure 13.** Deviated well pressure distribution field diagram after different development schemes. (**a**) scheme 1; (**b**) scheme 2; (**c**) scheme 3; (**d**) scheme 4; (**e**) scheme 5; (**f**) scheme 6; (**g**) scheme 7; (**h**) scheme 8; (**i**) scheme 9.

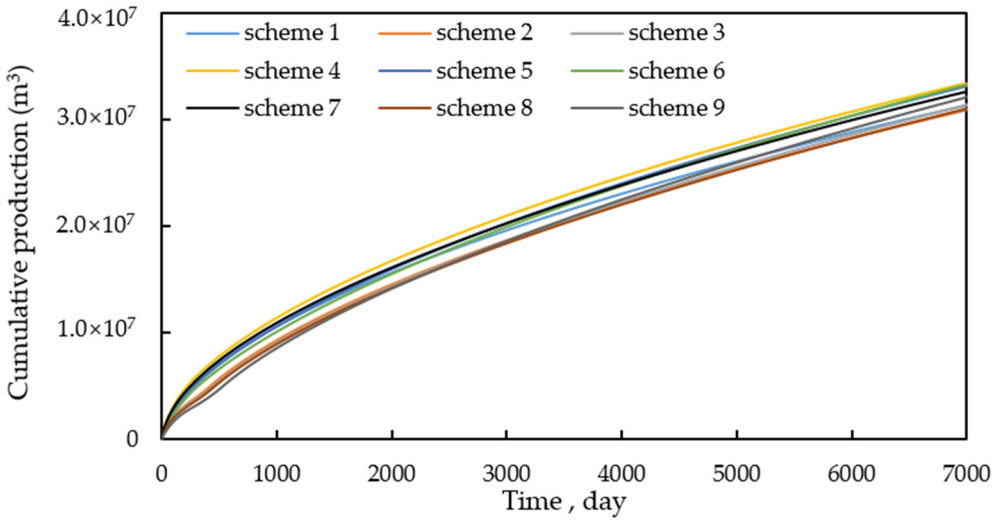


**Figure 14.** Cumulative gas production curve of single well after different development schemes of deviated well.

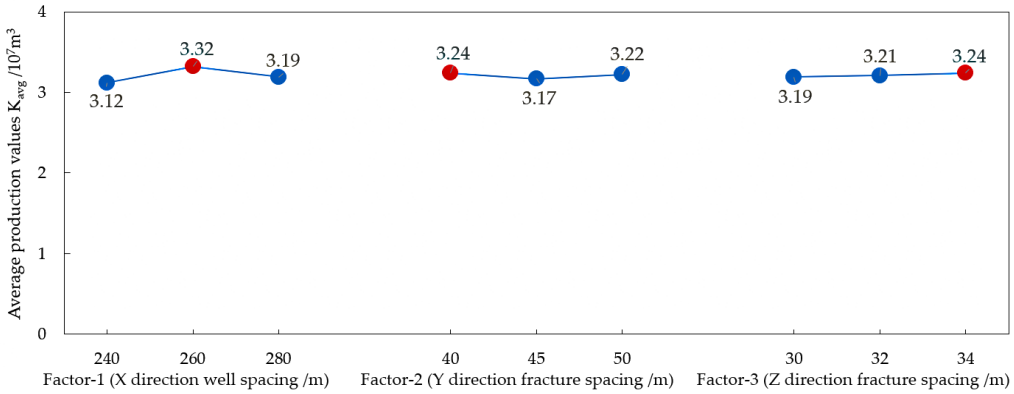


**Figure 15.** Mean value graph of each factor in deviated well.

**Table 8.** Orthogonal design table for vertical wells.

| Level | Factor | | |
|---|---|---|---|
| | **Factor 1**<br>**X Direction Well Spacing/m** | **Factor 2**<br>**Y Direction Well Spacing/m** | **Factor 3**<br>**Z Direction Fracture Spacing/m** |
| 1 | 240 | 40 | 30 |
| 2 | 260 | 45 | 32 |
| 3 | 280 | 50 | 34 |

According to the orthogonal design, nine schemes are simulated respectively. Figure 16 is the pressure distribution field of different development schemes after 20 years of exploitation, and Figure 17 is the cumulative production of a single well with different schemes of vertical wells.

Table 9 is the yield analysis table of the different schemes of deviated wells.

**Table 9.** Yield analysis table for different schemes of vertical wells.

| Orthogonal Design Table | | | | Well Yield $10^7$ $m^3$ |
|---|---|---|---|---|
| **Scheme** | **Factor-1** | **Factor-2** | **Factor-3** | |
| 1 | 1 | 1 | 1 | 1.12 |
| 2 | 1 | 2 | 2 | 1.02 |
| 3 | 1 | 3 | 3 | 0.98 |
| 4 | 2 | 1 | 2 | 1.11 |
| 5 | 2 | 2 | 3 | 1.16 |
| 6 | 2 | 3 | 1 | 1.13 |
| 7 | 3 | 1 | 3 | 1.23 |
| 8 | 3 | 2 | 1 | 1.18 |
| 9 | 3 | 3 | 2 | 1.25 |

According to the yield values of the above scheme, the average yield values, $K_{avg}$, of three levels in three factors are calculated respectively. As shown in Figure 18, the optimal combination of vertical well development is 280 m in the well spacing in the X direction, 40 m in the well spacing in the Y direction, and 30 m in the fracture spacing in the Z direction.

By calculating the range value, $R$, of three factors, for vertical wells, we get $R_{Factor\text{-}1}(0.18) > R_{Factor\text{-}2}(0.03) > R_{Factor\text{-}3}(0.02)$. Therefore, factor-1 (X direction well spacing) has the greatest impact on its productivity.

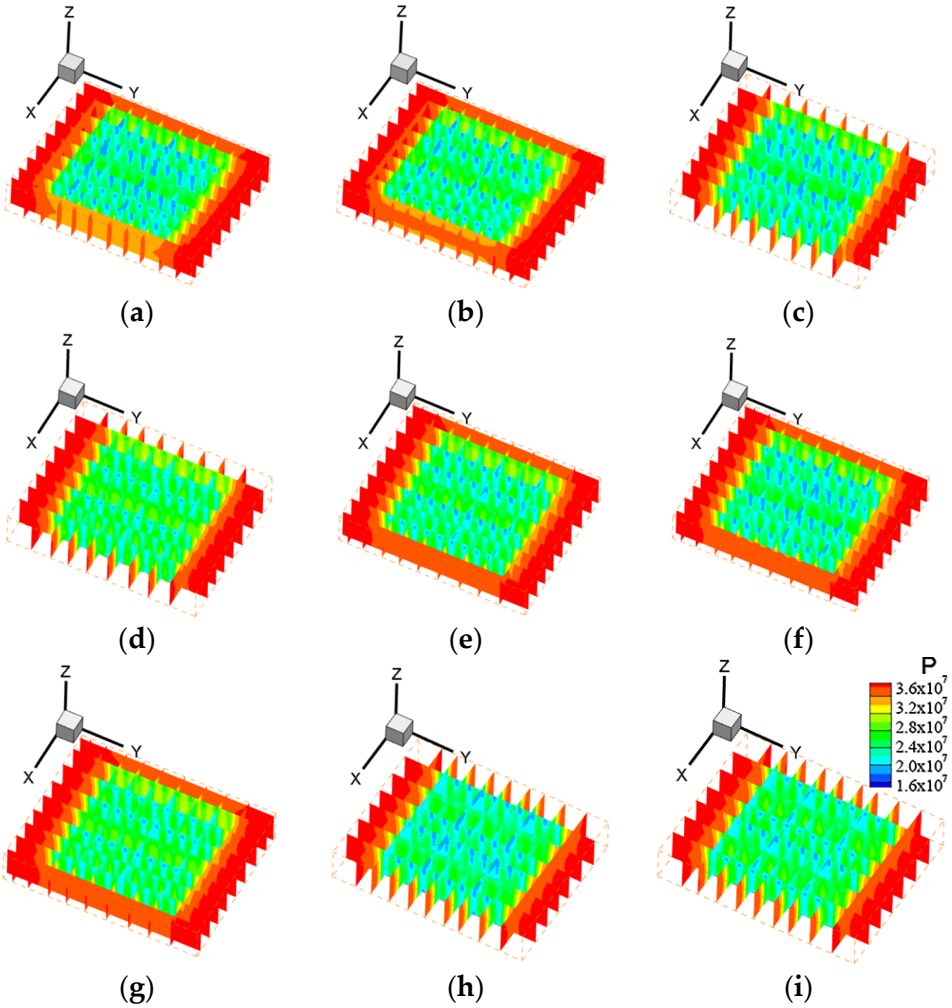


**Figure 16.** Vertical well pressure distribution field diagram after different development schemes. (**a**) scheme 1; (**b**) scheme 2; (**c**) scheme 3; (**d**) scheme 4; (**e**) scheme 5; (**f**) scheme 6; (**g**) scheme 7; (**h**) scheme 8; (**i**) scheme 9.

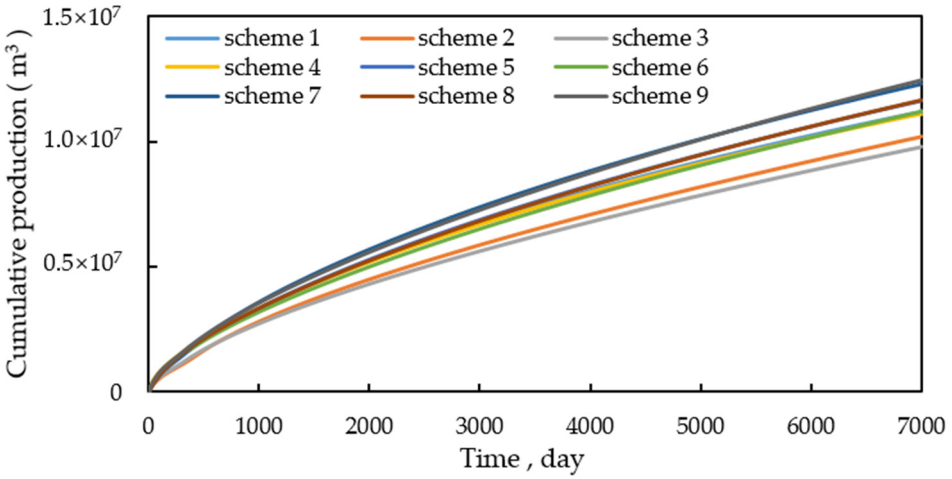


**Figure 17.** Cumulative gas production curve of single well after different development schemes of vertical well.

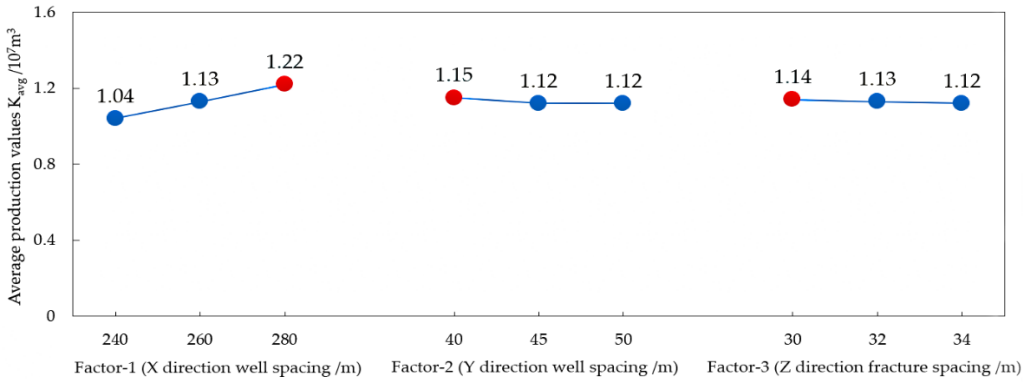


**Figure 18.** Mean value graph of each factor in vertical well.

## 6. Conclusions

In this paper, a gas–water two-phase flow model in a shale gas reservoir considering adsorption/desorption, Knudsen diffusion, and stress sensitivity are established. The fluid flow in fractures is modeled explicitly with the embedded discrete fracture model, and the reliability of the numerical model and algorithm is verified by comparing the actual production data of the Barnett shale gas reservoir.

After verification of the simulator, this paper first establishes a shale gas reservoir model with different natural fracture densities and simulates the production of the same horizontal well under different natural fracture densities. The results show that the natural fracture density will affect the utilization range of the well and then greatly affect the production of the well. The orthogonal experimental design method was then used to optimize the best combination of well spacing and fracture spacing for horizontal wells, deviated wells, and vertical wells. The results show that the optimal combination of horizontal well development is 260 m in the well spacing in the X direction, 50 m in the fracture spacing in the Y direction, and 34 m in the well spacing in the Z direction. The optimal combination of deviated well development is 260 m in the well spacing in the X direction, 40 m in the fracture spacing in the Y direction, and 34 m in the fracture spacing in the Z direction. The optimal combination of vertical well development is 280 m in the well spacing in the X direction, 40 m in the well spacing in the Y direction, and 30 m in the fracture spacing in the Z direction.

**Author Contributions:** Methodology, T.H.; Resources, Z.H.; Supervision, T.H.; Writing—original draft, X.L.; Writing—review & editing, F.S. and R.W. All authors have read and agreed to the published version of the manuscript.

**Funding:** This research was supported by the National Natural Science Foundation of China (No.52004246), the Natural Science Foundation of Zhejiang Province (No.LQ20E040003), and the Science and Technology Project of Zhoushan Bureau (No.2021C21016).

**Institutional Review Board Statement:** Not applicable.

**Informed Consent Statement:** Not applicable.

**Data Availability Statement:** Not applicable.

**Conflicts of Interest:** The authors declare no conflict of interest.

## References

1. Zhao, Y.; Tang, X.; Zhang, L.; Tang, H.M.; Tao, Z.W. Numerical solution of fractured horizontal wells in shale gas reservoirs considering multiple transport mechanisms. *J. Geophys. Eng.* **2018**, *15*, 739–750. [CrossRef]
2. Zhao, J.; Zhou, L.; Ma, J.; Li, Y. Numerical simulation study of fracturing wells for shale gas with gas–water two-phase flow system under desorption and diffusion conditions. *J. Nat. Gas Geosci.* **2016**, *1*, 251–256. [CrossRef]
3. Ghanizadeh, A.; Clarkson, C.; Aquino, S.; Ardakani, O.; Sanei, H. Petrophysical and geomechanical characteristics of Canadian tight oil and liquid-rich gas reservoirs: I. Pore network and permeability characterization. *Fuel* **2015**, *153*, 664–681. [CrossRef]

4. Cao, P.; Liu, J.; Leong, Y.K. A fully coupled multiscale shale deformation-gas transport model for the evaluation of shale gas extraction. *Fuel* **2016**, *178*, 103–117. [CrossRef]
5. Pollastro, R.M. Total petroleum system assessment of undiscovered resources in the giant Barnett Shale continuous (unconventional) gas accumulation, Fort Worth Basin, Texas. *AAPG Bull.* **2007**, *91*, 551–578. [CrossRef]
6. Zhongliang, C.; Mingqian, Z.H.U. Analysis of the combined model for the production decline of the shale-gas fractured horizontal well. *Pet. Geol. Oilfield Dev. Daqing* **2018**, *37*, 138–143.
7. Javadpour, F. Nanopores and apparent permeability of gas flow in mudrocks (shales and siltstone). *J. Can. Pet. Technol.* **2009**, *48*, 16–21. [CrossRef]
8. Xiong, X.; Devegowda, D.; Michel, G.G.; Sigal, R.F.; Civan, F. A fully-coupled free and adsorptive phase transport model for shale gas reservoirs including non-Darcy flow effects. In Proceedings of the SPE Annual Technical Conference and Exhibition, San Antonio, TX, USA, 8–10 October 2012.
9. Wang, J.; Liu, H.; Wang, L.; Zhang, H.; Luo, H.; Gao, Y. Apparent permeability for gas transport in nanopores of organic shale reservoirs including multiple effects. *Int. J. Coal Geol.* **2015**, *152*, 50–62. [CrossRef]
10. Wu, Y.S.; Li, J.; Ding, D.Y.; Wang, C.; Di, Y. A generalized framework model for the simulation of gas production in unconventional gas reservoirs. *SPE J.* **2014**, *19*, 845–857. [CrossRef]
11. Wang, F.P.; Reed, R.M.; John, A.; Katherine, G. Pore networks and fluid flow in gas shales. In Proceedings of the SPE Annual Technical Conference and Exhibition, New Orleans, LA, USA, 4–7 October 2009.
12. Bustin, R.M.; Bustin, A.M.M.; Cui, A.; Ross, D.; Pathi, V.M. Impact of shale properties on pore structure and storage characteristics. In Proceedings of the SPE Shale Gas Production Conference, Fort Worth, TX, USA, 16–18 November 2008.
13. Silin, D.; Kneafsey, T.J. Gas shale: From nanometer-scale observations to well modeling. In Proceedings of the Canadian Unconventional Resources Conference, Calgary, AB, Canada, 15–17 November 2011.
14. Liehui, Z.; Baochao, S.; Yulong, Z.; Jingjing, G.; Hongming, T. Establishment of apparent permeability model and seepage flow model for shale reservoir. *Lithol. Reserv.* **2017**, *29*, 108–118.
15. Ge, J.; Yao, H.B.; Wang, X.; Ye, Y.D.; Wang, J.L.; Wu, Z.Y.; Liu, J.W.; Fan, F.J.; Gao, H.L.; Zhang, C.L.; et al. Stretchable conductors based on silver nanowires: Improved performance through a binary network design. *Angew. Chem. Int. Ed.* **2013**, *52*, 1654–1659. [CrossRef] [PubMed]
16. Waters, G.A.; Dean, B.K.; Downie, R.C.; Kerrihard, K.J.; Austbo, L.; McPherson, B. Simultaneous hydraulic fracturing of adjacent horizontal wells in the Woodford Shale. In Proceedings of the SPE Hydraulic Fracturing Technology Conference, The Woodlands, TX, USA, 19–21 January 2009.
17. Kaiser, M.J. Haynesville shale play economic analysis. *J. Pet. Sci. Eng.* **2012**, *82*, 75–89. [CrossRef]
18. Rafiee, M.; Soliman, M.Y.; Pirayesh, E. Hydraulic fracturing design and optimization: A modification to zipper frac. In Proceedings of the SPE Annual Technical Conference and Exhibition, San Antonio, TX, USA, 8–10 October 2012.
19. De Souza, O.C.D.; Sharp, A.; Martinez, R.C.; Foster, R.A.; Simpson, M.R.; Piekenbrock, E.; Abou-Sayed, I. Integrated Unconventional Shale Gas Reservoir Modeling: A Worked Example From the Haynesville Shale, De Soto Parish, North Lousiana. In Proceedings of the SPE Americas Unconventional Resources Conference, Pittsburgh, PA, USA, 5–7 June 2012.
20. Yu, W.; Sepehrnoori, K. Optimization of multiple hydraulically fractured horizontal wells in unconventional gas reservoirs. *J. Pet. Eng.* **2013**. [CrossRef]
21. Ramanathan, V.; Boskovic, D.; Zhmodik, A.; Li, Q.; Ansarizadeh, M.; Michi, P.; Garcia, G. A Simulation Approach to Modelling and Understanding Fracture Geometry with Respect to Well Spacing in Multi Well Pads in the Duvernay—A Case Study. In Proceedings of the SPE/CSUR Unconventional Resources Conference, Calgary, AB, Canada, 20–22 October 2015.
22. Jiang, R.Z.; Yuan, J.W.; Cui, Y.Z.; Zhang, W.; Zhang, F.L.; Zhang, H.T.; Mao, N.Y. Productivity analysis of multi-fractured horizontal wells in shale gas reservoirs based on TPHM. *Nat. Gas Geosci.* **2019**, *30*, 95–101.
23. Yan, X.; Huang, Z.Q.; Yao, J.; Li, Y.; Fan, D.; Sun, H.; Zhang, K. An efficient numerical hybrid model for multiphase flow in deformable fractured-shale reservoirs. *SPE J.* **2018**, *23*, 1412–1437. [CrossRef]
24. Mahmoud, M. Development of a New Correlation of Gas Compressibility Factor (Z Factor) for High Pressure Gas Reservoirs. *J. Energy Resour. Technol.* **2014**, *136*, 012903. [CrossRef]
25. Beskok, A.; Karniadakis, G.E. Report: A model for flows in channels, pipes, and ducts at micro and nano scales. *Microscale Thermophys. Eng.* **1999**, *3*, 43–77.
26. Civan, F. Effective correlation of apparent gas permeability in tight porous media. *Transp. Porous Media* **2010**, *82*, 375–384. [CrossRef]
27. Song, W.; Yao, J.; Li, Y.; Sun, H.; Zhang, L.; Yang, Y.; Zhao, J.; Sui, H. Apparent gas permeability in an organic-rich shale reservoir. *Fuel* **2016**, *181*, 973–984. [CrossRef]
28. Zhang, R.; Ning, Z.F.; Yang, F.; Zhao, H.W.; Li-Hong, D.U.; Liao, X.W. Experimental study on microscopic pore structure controls on shale permeability under compaction process. *Nat. Gas Geosci.* **2014**, *25*, 1284–1289.
29. Ju, B.; Wu, Y.; Fan, T. Study on fluid flow in nonlinear elastic porous media: Experimental and modeling approaches. *J. Pet. Sci. Eng.* **2011**, *76*, 205–211. [CrossRef]
30. Xu, Y.; Cavalcante Filho, J.S.; Yu, W.; Sepehrnoori, K. Discrete-fracture modeling of complex hydraulic-fracture geometries in reservoir simulators. *SPE Reserv. Eval. Eng.* **2017**, *20*, 403–422. [CrossRef]

31. Yu, W.; Xu, Y.; Weijermars, R.; Wu, K.; Sepehrnoori, K. A numerical model for simulating pressure response of well interference and well performance in tight oil reservoirs with complex–fracture geometries using the fast embedded–discrete–fracture–model method. *SPE Reserv. Eval. Eng.* **2018**, *21*, 489–502. [CrossRef]
32. Liu, L.; Huang, Z.; Yao, J.; Di, Y.; Wu, Y.S. An efficient hybrid model for 3D complex fractured vuggy reservoir simulation. *SPE J.* **2020**, *25*, 907–924. [CrossRef]
33. Yan, X.; Huang, Z.; Zhang, Q.; Fan, D.; Yao, J. Numerical investigation of the effect of partially propped fracture closure on gas production in fractured shale reservoirs. *Energies* **2020**, *13*, 5339. [CrossRef]
34. Geng, L.; Li, G.; Wang, M.; Li, Y.; Tian, S.; Pang, W.; Lyu, Z. A fractal production prediction model for shale gas reservoirs. *J. Nat. Gas Sci. Eng.* **2018**, *55*, 354–367. [CrossRef]
35. Yu, W.; Sepehrnoori, K. Simulation of gas desorption and geomechanics effects for unconventional gas reservoirs. In Proceedings of the SPE Western Regional & AAPG Pacific Section Meeting 2013 Joint Technical Conference, Monterey, CA, USA, 19–25 April 2013.